The Astrophysical Journal, 945:20 (12pp), 2023 March 1 https://doi.org/10.3847/1538-4357/acb8ac

TESS Asteroseismic Analysis of HD 76920: The Giant Star Hosting an Extremely Eccentric Exoplanet

Chen Jiang (姜晨)[1], Tao Wu (吴涛)[2,3,4,5,6], Adina D. Feinstein[7,39], Keivan G. Stassun[8], Timothy R. Bedding[9,10], Dimitri Veras[11,12,13], Enrico Corsaro[14], Derek L. Buzasi[15], Dennis Stello[9,10,16], Yaguang Li (李亚光)[9,10], Savita Mathur[17,18], Rafael A. García[19], Sylvain N. Breton[14,20], Mia S. Lundkvist[21], Przemysław J. Mikołajczyk[22,23], Charlotte Gehan[1,24], Tiago L. Campante[24,25], Diego Bossini[24], Stephen R. Kane[26], Jia Mian Joel Ong (王加冕)[27], Mutlu Yıldız[28], Cenk Kayhan[29], Zeynep Çelik Orhan[28], Sibel Örtel[28], Xinyi Zhang (张昕旖)[30], Margarida S. Cunha[24,25], Bruno Lustosa de Moura[31,32], Jie Yu (余杰)[1], Daniel Huber[33], Jian-wen Ou (欧建文)[34], Robert A. Wittenmyer[35], Laurent Gizon[1,36,37], and William J. Chaplin[10,38]

[1] Max-Planck-Institut für Sonnensystemforschung, Justus-von-Liebig-Weg 3, D-37077 Göttingen, Germany; jiangc@mps.mpg.de
[2] Yunnan Observatories, Chinese Academy of Sciences, 396 Yangfangwang, Guandu District, Kunming, 650216, People's Republic of China; wutao@ynao.ac.cn
[3] Key Laboratory for the Structure and Evolution of Celestial Objects, Chinese Academy of Sciences, 396 Yangfangwang, Guandu District, Kunming, 650216, People's Republic of China
[4] Center for Astronomical Mega-Science, Chinese Academy of Sciences, 20A Datun Road, Chaoyang District, Beijing, 100012, People's Republic of China
[5] University of Chinese Academy of Sciences, Beijing 100049, People's Republic of China
[6] Institute of Theoretical Physics, Shanxi University, Taiyuan 030006, People's Republic of China
[7] Department of Astronomy and Astrophysics, University of Chicago, 5640 S. Ellis Avenue, Chicago, IL 60637, USA
[8] Department of Physics and Astronomy, Vanderbilt University, Nashville, TN 37235, USA
[9] Sydney Institute for Astronomy (SIfA), School of Physics, University of Sydney, NSW 2006, Australia
[10] Stellar Astrophysics Centre (SAC), Department of Physics and Astronomy, Aarhus University, Ny Munkegade 120, DK-8000 Aarhus C, Denmark
[11] Centre for Exoplanets and Habitability, University of Warwick, Coventry CV4 7AL, UK
[12] Centre for Space Domain Awareness, University of Warwick, Coventry CV4 7AL, UK
[13] Department of Physics, University of Warwick, Coventry CV4 7AL, UK
[14] INAF–Osservatorio Astrofisico di Catania, via S. Sofia 78, I-95123 Catania, Italy
[15] Department of Chemistry & Physics, Florida Gulf Coast University, 10501 FGCU Boulevard S., Fort Myers, FL 33965, USA
[16] School of Physics, University of New South Wales, NSW 2052, Australia
[17] Instituto de Astrofísica de Canarias (IAC), E-38205 La Laguna, Tenerife, Spain
[18] Universidad de La Laguna (ULL), Departamento de Astrofísica, E-38206 La Laguna, Tenerife, Spain
[19] Université Paris-Saclay & Université Paris Cité, CEA, CNRS, AIM, F-91191, Gif-sur-Yvette, France
[20] Université Paris Cité, Université Paris-Saclay, CEA, CNRS, AIM, F-91191, Gif-sur-Yvette, France
[21] Stellar Astrophysics Centre (SAC), Department of Physics and Astronomy, Aarhus University, Ny Munkegade 120, DK-8000 Aarhus C, Denmark
[22] Astronomical Observatory, University of Warsaw, Al. Ujazdowskie 4, 00-478 Warsaw, Poland
[23] Astronomical Institute, University of Wrocław, Mikołaja Kopernika 11, 51-622 Wrocław, Poland
[24] Instituto de Astrofísica e Ciências do Espaço, Universidade do Porto, Rua das Estrelas, 4150-762 Porto, Portugal
[25] Departamento de Física e Astronomia, Faculdade de Ciências da Universidade do Porto, Rua do Campo Alegre, s/n, 4169-007 Porto, Portugal
[26] Department of Earth and Planetary Sciences, University of California, Riverside, CA 92521, USA
[27] Department of Astronomy, Yale University, P.O. Box 208101, New Haven, CT 06520-8101, USA
[28] Department of Astronomy and Space Sciences, Science Faculty, Ege University, 35100, Bornova, İzmir, Türkiye
[29] Department of Astronomy and Space Sciences, Science Faculty, Erciyes University, 38030, Melikgazi, Kayseri, Türkiye
[30] State Key Laboratory of Lunar and Planetary Sciences, Macau University of Science and Technology, Macau, People's Republic of China
[31] Departamento de Fisica, Universidade Federal do Rio Grande do Norte, 59072-970 Natal, RN, Brazil
[32] Instituto Federal do Rio Grande do Norte-IFRN, Mossoró - RN, 59628-330, Brazil
[33] Institute for Astronomy, University of Hawai'i, 2680 Woodlawn Drive, Honolulu, HI 96822, USA
[34] School of Physics and Electromechanical Engineering, Shaoguan University, 512005 Shaoguan, Guangdong Province, People's Republic of China
[35] University of Southern Queensland, Centre for Astrophysics, USQ Toowoomba, QLD 4350, Australia
[36] Institut für Astrophysik, Georg-August-Universität Göttingen, Friedrich-Hund-Platz 1, D-37077 Göttingen, Germany
[37] Center for Space Science, NYUAD Institute, New York University Abu Dhabi, Abu Dhabi, UAE
[38] School of Physics and Astronomy, University of Birmingham, Birmingham B15 2TT, UK
Received 2022 December 21; revised 2023 February 1; accepted 2023 February 1; published 2023 March 2

Abstract

The Transiting Exoplanet Survey Satellite (TESS) mission searches for new exoplanets. The observing strategy of TESS results in high-precision photometry of millions of stars across the sky, allowing for detailed asteroseismic studies of individual systems. In this work, we present a detailed asteroseismic analysis of the giant star HD 76920 hosting a highly eccentric giant planet ($e = 0.878$) with an orbital period of 415 days, using five sectors of TESS light curve that cover around 140 days of data. Solar-like oscillations in HD 76920 are detected around 52 μHz by TESS for the first time. By utilizing asteroseismic modeling that takes classical observational parameters and stellar oscillation frequencies as constraints, we determine improved measurements of the stellar mass ($1.22 \pm 0.11\,M_{\odot}$),

[39] NSF Graduate Research Fellow.

radius ($8.68 \pm 0.34\,R_{\odot}$), and age (5.2 ± 1.4 Gyr). With the updated parameters of the host star, we update the semimajor axis and mass of the planet as $a = 1.165 \pm 0.035$ au and $M_{\rm p} \sin i = 3.57 \pm 0.22\,M_{\rm Jup}$. With an orbital pericenter of 0.142 ± 0.005 au, we confirm that the planet is currently far away enough from the star to experience negligible tidal decay until being engulfed in the stellar envelope. We also confirm that this event will occur within about 100 Myr, depending on the stellar model used.

Unified Astronomy Thesaurus concepts: Asteroseismology (73); Exoplanets (498); Red giant stars (1372)

1. Introduction

The excellent quality of photometric data from space observation missions, such as CoRoT (Baglin et al. 2006) and Kepler (Borucki et al. 2010), allow for major advancements in the understanding of stellar interior physics and evolution using asteroseismology. Asteroseismology is the study of the internal structure of stars by the interpretation of their oscillation frequencies. In particular, the detection of oscillations in solar-type and red giant stars has led to breakthroughs such as the discovery of fast core rotation (Beck et al. 2012) and a way to distinguish between hydrogen-shell-burning stars and stars that are also burning helium in their cores (Bedding et al. 2011).

The advent of space photometry has also brought in advancements in data analysis techniques (e.g., Corsaro & De Ridder 2014; Corsaro et al. 2015; Davies & Miglio 2016; Lund et al. 2017) and stellar modeling strategies (e.g., Wu & Li 2016, 2017; Serenelli et al. 2017; Silva Aguirre et al. 2017). Furthermore, by using individual oscillation frequencies as constraints in the model optimization process (Metcalfe et al. 2010; Jiang et al. 2011; Mathur et al. 2012; Paxton et al. 2013; Rendle et al. 2019), asteroseismic modeling has proven to be a robust tool to determine fundamental stellar properties, including stellar distances (Silva Aguirre et al. 2012; Rodrigues et al. 2014), radii, and masses (Casagrande et al. 2014; Pinsonneault et al. 2014; Sharma et al. 2016), and most importantly ages and core size for red giants and clump stars (Casagrande et al. 2016; Anders et al. 2017; Pinsonneault et al. 2018; Zhang et al. 2018, 2020). Consequently, this enables us to characterize systematically the properties of the exoplanet-host stars through asteroseismology, which in turn provides an unprecedented level of precision in the parameters estimated for the planets (Ballard et al. 2014; Campante et al. 2015; Lundkvist et al. 2016; Kayhan et al. 2019). Furthermore, the synergy between asteroseismology and exoplanetary research also enables us to set constraints on the spin–orbit alignment of exoplanet systems (Huber et al. 2013; Benomar et al. 2014; Chaplin et al. 2014; Lund et al. 2014; Campante et al. 2016a; Kamiaka et al. 2019) and to perform statistical inferences on the planetary orbital eccentricities, by making use of asterodensity profiling (Kane et al. 2012; Sliski & Kipping 2014; Van Eylen & Albrecht 2015; Van Eylen et al. 2019).

The Transiting Exoplanet Survey Satellite (TESS) Mission (Ricker et al. 2015) is NASA's near all-sky survey for exoplanets, which launched in 2018. The large sample of monitored systems guarantees the synergy between asteroseismology and exoplanetary science to continue to expand (Campante et al. 2018; Huber 2018; Hatt et al. 2023). TESS searches for exoplanets using the transit method in an area 400 times larger than that covered by the Kepler mission. Although the exploration of new exoplanetary systems is the main scientific goal of the mission, TESS has also provided aids toward the characterization of previously known systems (Kane et al. 2021). Thanks to the high-quality of TESS photometry and large sky coverage, oscillations are expected to be detected in hundreds of thousands of solar-like oscillators (Campante et al. 2018; Huber 2018; Schofield et al. 2019), including several hundred asteroseismic exoplanet hosts (Campante et al. 2016b). Detections of oscillations by TESS in previously known exoplanet-host stars have been reported by several works (e.g., Campante et al. 2019; Jiang et al. 2020b; Nielsen et al. 2020; Hill et al. 2021; Huber et al. 2022), following on the discovery of the first planet transiting a star (TOI-197) in which oscillations could be measured by TESS (Huber et al. 2019). These extraordinary synergies between asteroseismology and exoplanetary science significantly improve our understanding of planet systems outside of the solar system and provide insight into the occurrence rates of exoplanets as a function of their host stars' property and evolutionary state, as well as the planets' mass, size, and orbital architecture. One of the most interesting architectures is the planets having very eccentric orbits that are considered as a possible origin of hot Jupiter (see Dawson & Johnson 2018, for a review). Planets in very eccentric orbits are a prime example and testbed of how planetary systems form and evolve.

The first planet discovered to orbit around an evolved giant star, ι Draconis b, is on a highly eccentric orbit with $e = 0.71$ (Frink et al. 2002; Kane et al. 2010). Even larger orbital eccentricity is found in a planet around the giant star HIP 126844 with $e = 0.76$ (Adamów et al. 2012, 2018). In this work, using TESS data, we present an asteroseismic analysis of the K giant star HD 76920 (TIC 302372658) known to host a planet. At the time that HD 76920b was first detected through the radial-velocity (RV) survey of the Pan-Pacific Planet Search (Wittenmyer et al. 2017), it was the most eccentric exoplanet known to orbit an evolved star, with an orbital eccentricity of 0.856 ± 0.009. Later, with the help of new multi-site RV measurements, Bergmann et al. (2021) refined the planetary properties, finding an even higher eccentricity of 0.8783 ± 0.0025 and an orbital period of $415.891^{+0.043}_{-0.039}$ days, a minimum planet mass of $3.13^{+0.41}_{-0.43}\,M_{\rm Jup}$, and a semimajor axis of $1.091^{+0.068}_{-0.077}$ au. There is no evidence of any unseen binary companion, suggesting a scattering event rather than Kozai oscillations as the probable explanation for the observed eccentricity, and making the system valuable to the study of the evolution and occurrence of planets around evolved stars. TESS detected solar-like oscillations in HD 76920 for the first time. Bergmann et al. (2021) analyzed three sectors (9, 10, and 11) of TESS data and estimated the stellar mass and radius through the scaling relations (Brown et al. 1991; Kjeldsen & Bedding 1995; Stello et al. 2008; Kallinger et al. 2010) using the measurements of global seismic parameters. While the scaling relations provide decent estimates of the stellar mass and radius for stars showing solar-like oscillations, improvements, in terms of accuracy and precision, of the estimates can be achieved by using asteroseismic modeling and individual oscillation modes.

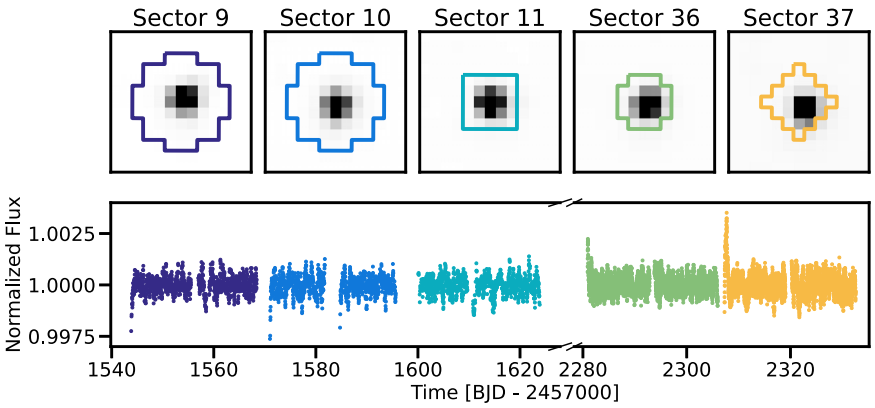

Figure 1. `eleanor` best-fit apertures (top) overlaid on the TESS target pixel files (TPFs) extracted per each sector. The TPFs are all scaled from 0–30,000 e^{-1} s^{-1}. We use these apertures to extract the flux within `eleanor`, which are then corrected via the default `eleanor` corrected flux routine (bottom). Apertures and light curves are colored by TESS sector.

In this paper, we aim to analyze the solar-like oscillations from five sectors of the TESS photometric light curve. Including these oscillations in detailed stellar modeling can help us derive precise fundamental stellar properties of the host star. The improved stellar parameters can further be used to update the properties of the orbiting planet, which is of great importance in characterizing the planetary system. The determined stellar age from asteroseismology and modeling provides information about the evolution of the system, which assists in predicting the final fate of the planet.

2. Observations

2.1. TESS Observations

HD 76920 has been observed by TESS in Sectors 9–11 at a 30 minute cadence during its Cycle 1 observations, and Sectors 36 and 37 at a 10 minute cadence[40] during its Cycle 3 observations. To extract these light curves, we used the open-source Python package `eleanor` (v2.0.3; Feinstein et al. 2019).[41] `eleanor` performs background subtraction, systematics corrections, and aperture selection per each sector of data. We extracted 13×13 pixels postage stamps and applied the `eleanor` default apertures for light curve extraction (top panel of Figure 1). Although the aperture selection process is optimized for exoplanet searches, we found also these default apertures to perform well for asteroseismic measurements.

We used the `eleanor` corrected flux; this flux option corrects for systematic issues by regressing against a linear model of time, background, and position and removing trends by the co-trending basis vectors provided by the Science Process Operations Center pipeline (Jenkins et al. 2016). We additionally applied quality masks, provided by `eleanor`, to remove any bad cadences and removed outliers $\geqslant 7\sigma$ from the median of each light curve. The resulting light curves are shown in the bottom panel of Figure 1. No transit of the planet was detected in existing TESS data due to the short observation coverage compared to its long orbital period. TESS is expected to observe HD 76920 again for 5 months in Cycle 5.

[40] HD 76920 has also been observed in Sector 38 at a 10 minute cadence, but the data was not released at the time of this analysis.

[41] For sectors 36 and 37, `eleanor` uses the `TessCut` tool (Brasseur et al. 2019).

2.2. Broadband Photometry and Spectral Energy Distribution

As an independent determination of the basic stellar parameters, we performed an analysis of the broadband spectral energy distribution (SED) of the star together with the Gaia DR3 parallax (with no systematic offset applied; see, e.g., Stassun & Torres 2021), in order to determine an empirical measurement of the stellar radius, following the procedures described in Stassun & Torres (2016) and Stassun et al. (2017, 2018a). We pulled the $B_T V_T$ magnitudes from Tycho-2, the JHK_S magnitudes from the Two Micron All Sky Survey, the W1–W4 magnitudes from the Wide-field Infrared Survey Explorer, and the $G_{BP} G_{RP}$ magnitudes from Gaia DR3. Together, the available photometry spans the full stellar SED over the wavelength range of 0.4–22 μm (see Figure 2).

We performed a fit using Kurucz stellar atmosphere models, with the effective temperature ($T_{\rm eff}$), surface gravity ($\log g$), and metallicity ([Fe/H]) adopted from the spectroscopic analysis of Wittenmyer et al. (2017). The remaining free parameter is the extinction A_V, which we limited to the maximum line-of-sight extinction from the Galactic dust maps of Schlegel et al. (1998). The resulting fit (Figure 2) has a reduced χ^2 of 2.2, and best-fit $A_V = 0.20 \pm 0.05$. Integrating the (unreddened) model SED gives the bolometric flux at Earth, $F_{\rm bol} = 3.12 \pm 0.11 \times 10^{-8}$ erg s^{-1} cm^{-2}. Taking the $F_{\rm bol}$ and $T_{\rm eff}$ together with the Gaia parallax, gives the stellar radius, $R_\star = 8.64 \pm 0.37\, R_\odot$, revealing the star to be clearly evolved. In addition, we can estimate the stellar mass directly from $R_\star$ together with the spectroscopic $\log g$ from Wittenmyer et al. (2017, see Table 1), which gives $M_\star = 2.37 \pm 0.41\ M_\odot$; this is higher than the value obtained from the empirical relations of Torres et al. (2010), giving $M_\star = 1.68 \pm 0.10\ M_\odot$, indicating an overestimate of spectroscopic $\log g$ (see Section 4). Combining $F_{\rm bol}$ and Gaia DR3 parallax allows us to derive a luminosity of $L_\star = 32.54 \pm 1.17\, L_\odot$. We also performed an independent SED fitting using the SEDEX pipeline (Yu et al. 2021, 2023) with MARCS atmosphere models (Gustafsson et al. 2008) and the same input atmospheric parameters. The resulting parameters from both SED fittings are well consistent, as listed in Table 1.

3. Asteroseismic Analysis

3.1. Global Oscillation Parameters

For the seismic analysis, the TESS light curve prepared by `eleanor` was distributed to several groups using different

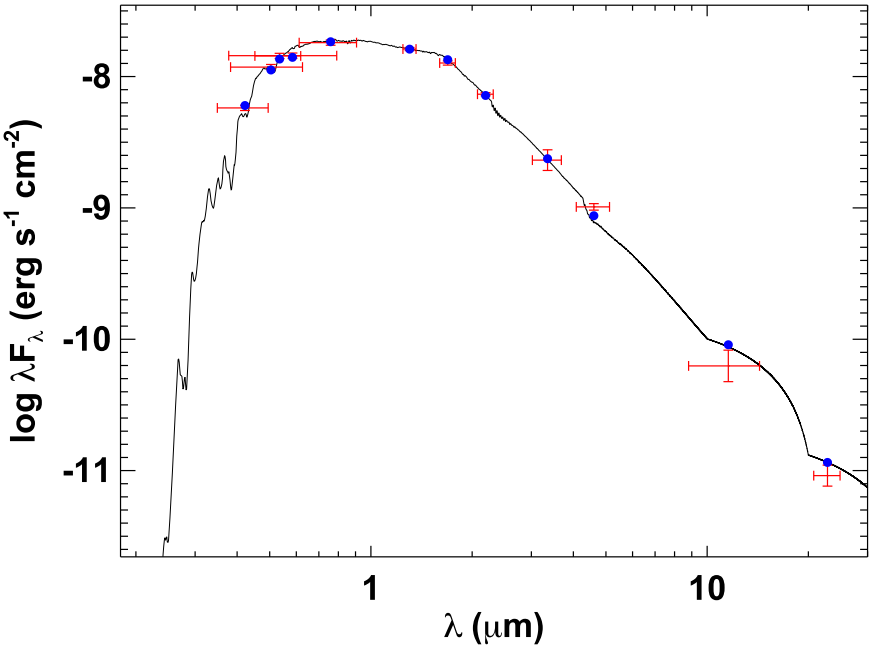

Figure 2. SED of HD 76920. Red symbols represent the observed photometric measurements, whereas the horizontal bars represent the effective width of the passband. Blue symbols are the model fluxes from the best-fit Kurucz atmosphere model (black).

pipelines (e.g., Huber et al. 2009; Mathur et al. 2010; Jiang et al. 2011; Lundkvist 2015; Campante et al. 2017; Yu et al. 2018; Corsaro et al. 2020; De Moura et al. 2020; Li et al. 2020) to extract the seismic parameters. Figure 3 shows the power density spectrum of HD 76920 computed based on the `eleanor` light curve, combining both Cycle 1 and Cycle 3 data. The 10 minute cadence sectors were rebinned to 30 minute cadence, with a simple average over three measurements. The power spectrum shows a frequency-dependent background signal due to stellar activity, granulation, and faculae that can be modeled by a superposition of several Lorentzian-like functions (i.e., Harvey-like models, Harvey 1985; Karoff 2008; Jiang et al. 2011; Kallinger et al. 2014; Corsaro et al. 2017), and a white noise term. The background shown as the cyan dotted curve in Figure 3 was obtained by fitting the background model with two Harvey-like components and one white noise to the smoothed power spectrum. The target pixel time series of the Cycle 3 sectors have been detrended with a moving median to remove long timescale stellar variations. As a result, the background noise at low frequency is greatly suppressed during this process. Therefore, the background fit displayed in Figure 3 disregarded frequencies below $\sim$10 μHz. The global seismic parameters such as the frequency of maximum power ($\nu_{\rm max}$) and the mean large frequency separation ($\Delta\nu$) were based on the analysis of the background-corrected power spectrum generated by each group.

In general, $\nu_{\rm max}$ was measured by fitting a Gaussian distribution profile to the power excess hump of the smoothed power spectrum (e.g., Hekker et al. 2010) or through the 2D autocorrelation function (e.g., Viani et al. 2019). To measure $\Delta\nu$, techniques like autocorrelation of the amplitude spectrum (e.g., Huber et al. 2009; Mosser & Appourchaux 2009), power spectrum of the power spectrum (e.g., Kjeldsen & Bedding 1995; Mathur et al. 2010; Jiang 2015), matched filter response function (e.g., Gilliland et al. 2011), and asymptotic or linear fit to the frequencies of the radial modes (individual mode extraction given in Section 3.2) were used. However, a clear shift of the oscillation power excess region to lower frequencies is observed in the power spectrum generated with Cycle 3 data (Sectors 36 and 37), compared with the Cycle 1 one (Sectors 9–11), as illustrated in the upper panel of Figure 4. This is principally due to the stochastic nature of the oscillations so that the change in mode amplitudes impacts the value of $\nu_{\rm max}$. This shift of the power excess region may lead to a larger uncertainty in $\nu_{\rm max}$ when compared to the corresponding formal uncertainty originating from different pipelines. With this in mind, we computed consolidated results from the eight independent determinations of the global seismic parameters. In particular, we adopted the mean values of the parameter estimates returned by all methods and recalculated the uncertainties by adding in quadrature the corresponding formal uncertainty and the standard deviation. The consolidated results are $\nu_{\rm max} = 53.2 \pm 2.3$ μHz and $\Delta\nu = 5.53 \pm 0.15$ μHz. We note that due to the intrinsic change of the distribution of mode amplitudes observed between Cycle 1 and Cycle 3 data, this uncertainty of $\Delta\nu$ resulting from our statistical consolidation approach, can also be overestimated and can be decreased by examining the different $\Delta\nu$ values against the échelle diagrams (Stello et al. 2011). As an alternative, instead of taking into account the scatter across results, we also quote here the pipeline results that are of the smallest deviation from the mean values of all pipeline results as $\nu_{\rm max} = 52.4 \pm 0.3$ μHz and $\Delta\nu = 5.52 \pm 0.02$ μHz, considering both parameters simultaneously (i.e., both parameters returned by the same pipeline). This level of uncertainty of $\Delta\nu$ is of comparable magnitude to those extracted from two sectors of TESS observations of red giants (Silva Aguirre et al. 2020). The combined power spectrum corrected from the background model is shown in the bottom panel of Figure 4, where signals with $\nu < 50$ μHz are largely enhanced by the Cycle 3 data, and those with $\nu > 50$ μHz are due to the Cycle 1 data. The asteroseismic analysis discussed in Section 3 was performed based on the combined power spectrum (lower panel of Figure 4).

Table 1
Stellar Parameters of HD 76920

Parameter	Value	References
	Basic Properties	
TIC	302372658	1
Hipparcos ID	43803	2
TESS mag	6.87	1
Sp. type	K1 III	3
	Spectroscopy	
$T_{\rm eff}$ (K)	4698 ± 100	4
	4664 ± 53	5
[Fe/H] (dex)	-0.11 ± 0.10	4
	-0.19 ± 0.06	5
$\log g$ (cgs)	2.94 ± 0.15	4
	2.71 ± 0.04	5
	SED and Gaia DR3 Parallax[a]	
π (mas)	5.4618 ± 0.0187	6
A_V	0.20 ± 0.05	7
	0.15 ± 0.07	7
$F_{\rm bol}$ (erg s^{-1} cm^{-2})	$(3.12 \pm 0.11) \times 10^{-8}$	7
	$(3.08 \pm 0.11) \times 10^{-8}$	7
$R_\star$ ($R_\odot$)	8.64 ± 0.37	7
	8.70 ± 0.25	7
$L_\star$ ($L_\odot$)	32.54 ± 1.17	7
	32.06 ± 1.16	7
$M_\star$ ($M_\odot$)	1.68 ± 0.10[b]	7
	Asteroseismology	
$\Delta\nu$ (μHz)	5.53 ± 0.15	7
$\nu_{\rm max}$ (μHz)	53.2 ± 2.3	7
$M_{\star,\rm seis}$ ($M_\odot$)	1.22 ± 0.11	7
$R_{\star,\rm seis}$ ($R_\odot$)	8.68 ± 0.34	7
ρ (gcc)	0.0026 ± 0.0004	7
$\log g$ (cgs)	2.648 ± 0.037	7
t (Gyr)	5.2 ± 1.4	7

Notes.
[a] Two SED pipelines are used to obtain A_V, $F_{\rm bol}$, $R_\star$, and $L_\star$ (Section 2.2). The second value of each parameter is from the SEDEX pipeline (Yu et al. 2021, 2023).
[b] Based on extrapolated relations of Torres et al. (2010).
References. (1) Stassun et al. (2018b), (2) van Leeuwen (2007), (3) Houk & Cowley (1975), (4) Wittenmyer et al. (2017), (5) Bergmann et al. (2021), (6) Gaia Collaboration et al. (2021), (7) this work.

3.2. Individual Mode Frequencies

In the bottom panel of Figure 4, the combined power spectrum shows a regular series of peaks corresponding to solar-like oscillations within the frequency range between 30 and 80 μHz. To extract individual oscillation modes from the power spectrum several independent methods ranging from traditional iterative fitting of sine waves, i.e., pre-whitening (e.g., Kjeldsen et al. 2005; Lenz & Breger 2005; Bedding et al. 2007; Jiang et al. 2011), to fitting of Lorentzian mode profiles individually or in a global power spectrum model (e.g., Handberg & Campante 2011; Appourchaux et al. 2012; Mosser et al. 2012; Corsaro et al. 2015, 2020; Vrard et al. 2015; Davies & Miglio 2016; Handberg et al. 2017; Roxburgh 2017; Kallinger et al. 2018; Li et al. 2020; Breton et al. 2022) were used by different pipelines. The extracted mode frequencies and corresponding uncertainties are listed in Table 2. The extracted radial modes also allowed us to measure $\Delta\nu$ by fitting a straight line to the radial-mode frequencies. Thus, the slope of the line is $\Delta\nu$ is 5.62 ± 0.03 μHz using this method. The échelle diagram (Bedding & Kjeldsen 2010) generated using this $\Delta\nu$ is depicted in Figure 5. The two vertical ridges located near the right edge of the figure correspond to the $\ell = 0$ (red circles) and 2 (blue triangles) modes. However, due to the relatively short duration of our TESS data for HD 76920, a clear mixed-mode pattern is not visible in the power spectrum or in the échelle diagram, though there are a few peaks corresponding to the $\ell = 1$ mixed modes (green diamonds in Figure 5) appearing in the spectrum. In Table 2, we also list the $\ell = 1$ modes that are extracted by at least two independent sources, including a pair of mixed modes around 53 μHz that were simultaneously extracted by three independent sources.

4. Asteroseismic Modeling

Asteroseismic modeling is a powerful tool to estimate fundamental stellar properties. Five independent teams performed modeling efforts to search for the stellar models that best match the classical and asteroseismic constraints from observations for HD 76920. These teams employed different stellar evolution codes (`ASTEC`, `MESA`; Christensen-Dalsgaard 2008a; Paxton et al. 2011, 2013, 2015), oscillation codes (`ADIPLS`, `GYRE`; Christensen-Dalsgaard 2008b; Townsend & Teitler 2013), and optimization methods (Mier 2017; Kayhan et al. 2019; Wu & Li 2019; Yıldız et al. 2019; Jiang & Gizon 2021; Zhang et al. 2022). The input physics adopted by each team is detailed in Table 3. Diffusion and overshoot were turned off by the teams, with the exception of one team. For the modeling, all five teams used the luminosity $L_\star$ of $32.54 \pm 1.17\,L_\odot$ derived with Gaia DR3 parallax (Section 2.2) and the spectroscopic measurements, i.e., the effective temperature $T_{\rm eff}$ and metallicity [Fe/H] from Wittenmyer et al. (2017), as constraints. As for the seismic constraints, the large frequency separation $\Delta\nu = 5.52 \pm 0.02$ μHz and $\ell = 0$ and 2 mode frequencies in Table 2 were used[42]. Generally, the most p-dominated $\ell = 2$ mixed modes of each model were selected to be compared with the observations, except for team Ong who computed the pure quadrupole p-modes of stellar models using the π-mode isolation condition in Ong & Basu (2020) as implemented in GYRE[43]. The constraint on $\nu_{\rm max}$ was not considered in the modeling due to the discrepancy of the oscillation power excess region between the sectors (Section 3.1). We measured the phase shift $\epsilon_{\rm c}$ of the central radial mode, which is the linear offset in the asymptotic fit to the acoustic modes, as $\sim$0.94, indicating that the star is still on the red giant branch (RGB) burning only hydrogen in a shell because the more evolved horizontal branch stars (e.g., red clump and secondary clump stars) that have already ignited helium in the core would have a systematically smaller $\epsilon_{\rm c}$ than their counterparts on the RGB (Kallinger

[42] The identified five $\ell = 1$ modes listed in Table 2 do not show a clear pattern of mixed modes, thus, providing very limited constraints on the models, as one can always find a match to the observed mode among the dense theoretical dipolar modes.
[43] These pure quadrupole p-modes are matched to the frequencies of the observed p-dominated quadrupole mixed modes, under the assumption that interference from mode mixing in these high-luminosity red giants may be neglected (see discussion in Ong et al. 2021).

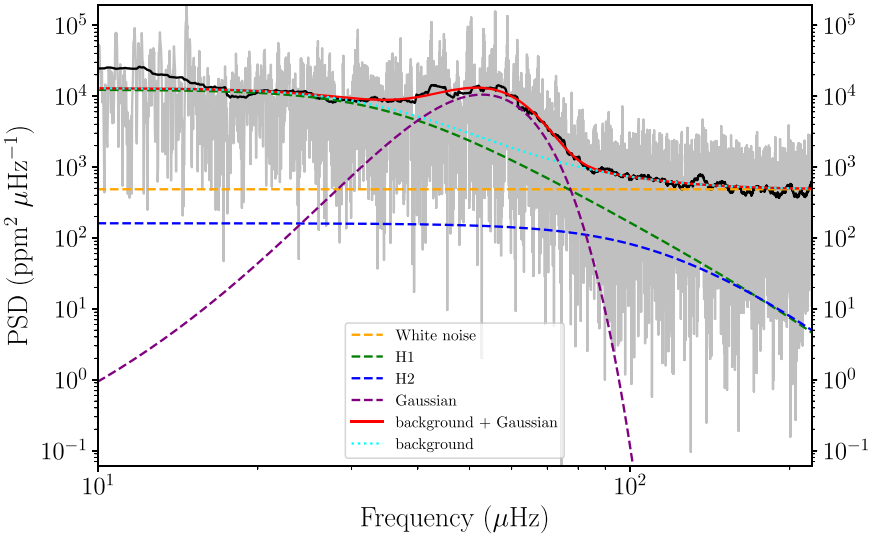

Figure 3. Power spectral density (PSD) of HD 76920 and corresponding global background model fit (cyan dotted curve). The background model consists of two Harvey-like profiles (green and blue dashed curves) and white noise (orange dashed line). The solid red curve depicts the summation of the background and a Gaussian fit (purple dashed) to the oscillation power excess envelope. The PSD is generated using five sectors of TESS data (Figure 1). The 10 minute cadence sectors are rebinned to 30 minute cadence, with a simple average over three measurements. The original PSD is shown in gray and a heavily smoothed (Gaussian with an FWHM of $\Delta\nu$) version in black. The fit displayed here disregarded frequencies below $\sim$10 μHz (Section 3.1).

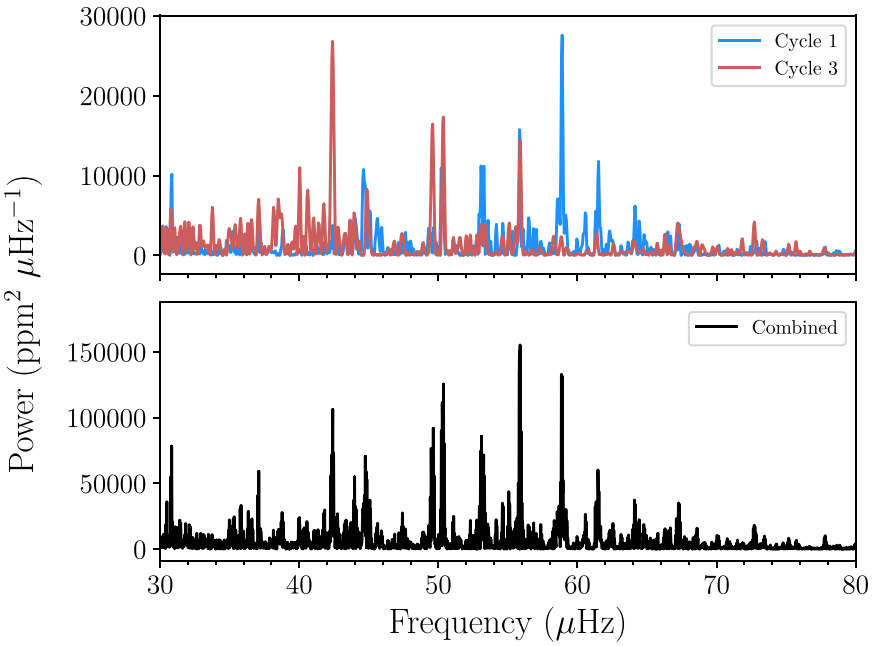

Figure 4. Background-corrected power spectra of HD 76920 depicted in the power excess region. Top panel: power spectra of the Cycle 1 (Sectors 9–11) and Cycle 3 (Sectors 36 and 37) light curve. The Cycle 1 data shows a larger value of $\nu_{\rm max}$, compared with the Cycle 3 data. Bottom panel: power spectra of the combined light curve that is used for the asteroseismic analysis.

et al. 2012). Moreover, horizontal branch tracks hardly cross the observational constraints in the H-R diagram; thus, we limited the modeling only to the RGB.

The outputs from the five teams are generally in agreement with each other (Table 4), though differences are inevitably seen due to the diversity of modeling codes, procedures, and input physics adopted by different teams. We note that the amount of convective overmixing ($f_{\rm ov} = 0.006$) adopted by team Ong is mainly for numerical softening and is too small to induce an appreciable physical difference in the spectroscopic parameters (see discussions in, e.g., Claret & Torres 2017, 2018, 2019; Guo & Li 2019; Zhang et al. 2022). Furthermore, since we have only used even-degree ($\ell = 2$) p-dominated modes in this work, the effects of overshoot on the g-mode cavity (e.g., Lindsay et al. 2022) are not relevant. For the even-degree p-modes, envelope overshoot will reduce the amplitude of the convective-glitch signature induced into the p-modes, which is already very small on the main sequence, and decreases in amplitude as the convective boundary retreats closer to the core as the star ascends the RGB. The consolidated values (the mean from all sources) for stellar mass $M_{\star,\rm seis}$, radius $R_{\star,\rm seis}$, age t, surface gravity $\log g$, and density ρ are summarized in Table 1, constraining the corresponding parameters to a precision level of 9%, 4%, 27%, 1%, and 15%, respectively, which are the most precise results for HD 76920 so far. The final uncertainties on these stellar parameters were recalculated by adding in

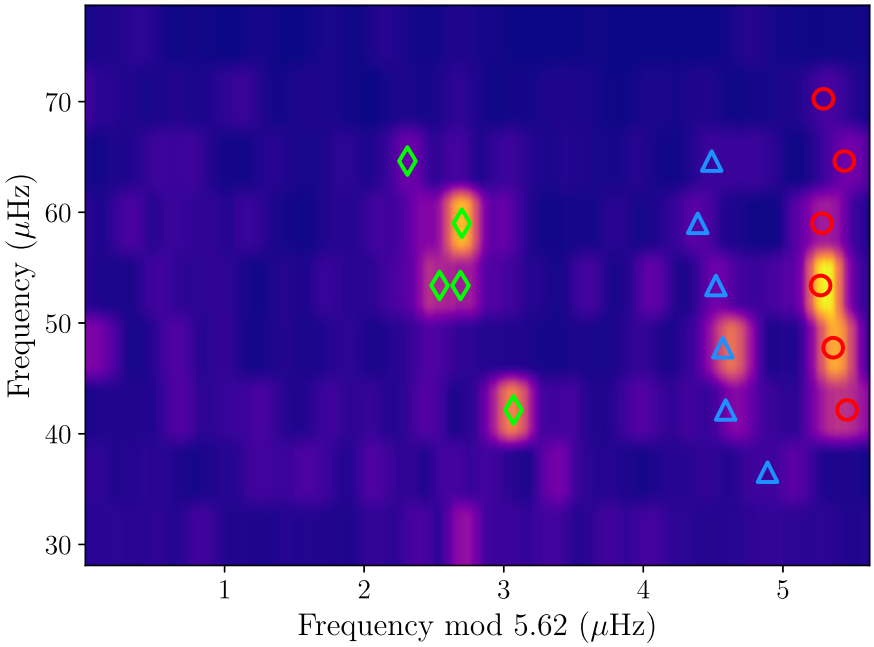

Figure 5. Échelle diagram of the background-corrected PSD, folded on a large frequency separation of $\Delta\nu = 5.62$ μHz estimated by fitting the radial-mode frequencies (see Section 3.2). Identified individual mode (Table 2) frequencies are marked with red circles ($\ell = 0$), green diamonds ($\ell = 1$), and blue triangles ($\ell = 2$).

Table 2
Extracted Oscillation Frequencies from the TESS Light Curve and Mode Identification Based on the Best-fitting Model for HD 76920

ℓ	$n(n_p)$	ν (μHz)	σ_ν (μHz)	S/N
0	7	44.80	0.13	6.63
0	8	50.32	0.10	8.08
0	9	55.85	0.08	12.50
0	10	61.48	0.08	6.71
0	11	67.18	0.13	3.83
0	12	72.73	0.15	4.0
1	6	42.41	0.08	12.05
1	8	53.12	0.03	9.54
1	8	53.27	0.03	6.73
1	9	58.90	0.07	6.95
1	10	64.13	0.08	3.61
2	5	38.61	0.29	3.71
2	6	43.93	0.24	5.88
2	7	49.53	0.12	7.13
2	8	55.10	0.07	5.42
2	9	60.59	0.20	4.48
2	10	66.32	0.07	3.89

Note. Each mode is labeled according to its mode degree ℓ, radial order n (or radial order of acoustic-component n_p for non-radial modes) from the best-fitting model. ν and σ_ν are the mode cyclic frequency and uncertainty. Modes identified simultaneously by at least two independent methods/sources are selected and used as modeling constraints. All these modes have a signal-to-noise ratio (S/N) larger than 3. The noise at each frequency is calculated as the average amplitude in the residual periodogram in a frequency range (20 μHz box size) that encloses the mode peak after the frequency is pre-whitened.

quadrature the corresponding formal uncertainty for a given parameter to the standard deviation of the parameter estimates returned by all teams. Therefore, both random and systematic errors arising from the diversity of modeling methods from different teams were taken into account. The estimated $\log g$ from modeling is distinctly smaller than the spectroscopic results reported by Wittenmyer et al. (2017), but matches the one measured by Bergmann et al. (2021) (who used updated spectroscopy data) within 1σ, confirming the SED results (see Section 2.2).

Figure 6 shows the locations of the sampling points by BESTP in the H-R diagram, along with a series of evolutionary tracks with different initial masses generated by ASTEC. The sampling points are color coded according to the normalized likelihood; thus, redder samples have higher possibilities of being the representation of the real star. According to the figure, HD 76920 is most likely approaching close to the RGB luminosity bump, where the properties of mixed modes are significantly impacted by the buoyancy glitch (Cunha et al. 2015, 2019; Jiang et al. 2020a), a signature that can help us inspect the stellar mid-layer structures (Pinćon et al. 2020; Jiang et al. 2022). However, the short observation duration for HD 76920 limits the detection of mixed modes from the TESS power spectrum; thus, such investigation of stellar interior structure with the help of mixed modes is not feasible with current TESS data. Nevertheless, by matching the theoretical oscillation frequencies calculated for the best-fitting model with the observed TESS power spectrum (Figure 7), we could confirm the mode degree and identify the mode order for the oscillation modes that were extracted by different groups (Table 2). The theoretical modes used to identify observed modes are corrected for the surface effect (e.g., Houdek et al. 2017) that yields a systematic offset between the calculated and the observed oscillation frequencies. For theoretical dipolar mixed modes, correction for the surface effect was not performed due to the lack of enough observed dipolar frequencies; thus, we did not show them in Figure 7.

5. Characterization of HD 76920 b

According to the prediction for the transit ephemeris made by Bergmann et al. (2021), if HD 76920b were to transit, it would have done so during TESS Sector 9. However, no clear

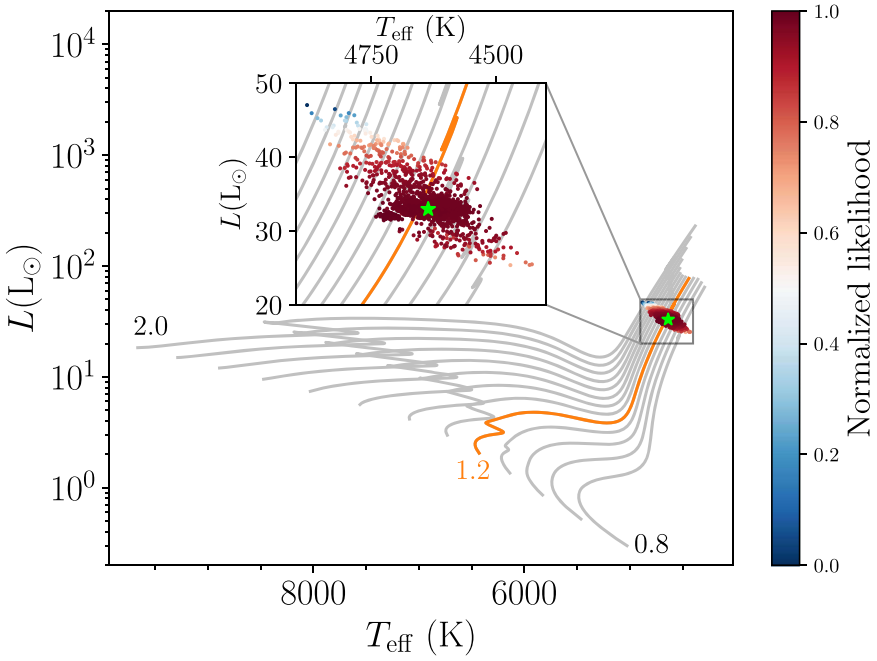

Figure 6. Evolutionary tracks for a series of ASTEC models with different initial masses but the same chemical abundance ($X = 0.714$ and $Z = 0.0142$, corresponding to [Fe/H] $= -0.09$) and mixing length parameter ($\alpha = 1.927$) that are the optimization outputs of the BESTP pipeline. The initial masses of the models increase from 0.8–2.0 $M_\odot$ with a step of 0.1 $M_\odot$. The evolutionary track indicated by orange is with an initial mass of 1.2 $M_\odot$, which is closest to the adopted value (Table 1). Sampling points by BESTP are drawn in the diagram and also in the inset, with color-coded normalized likelihood values. The green star marks the location of our best-fitting model ($M = 1.21\ M_\odot$, $X = 0.713$, and $Z = 0.0145$) from BESTP.

Table 3
Modeling Configurations from Different Sources

Team	Ong	Kayhan	Izmir	Zhang	BESTP
Evolution code	MESA (r12778)	MESA (r12778)	MESA (r15140)	MESA (r10398)	ASTEC
Oscillation code	GYRE	ADIPLS	ADIPLS	ADIPLS	ADIPLS
EoS[a]	MESA/OPAL	MESA/OPAL	MESA/OPAL	MESA/OPAL	OPAL
Surface correction[b]	BG-2term	KB	KB	None	BG-2term
Nuclear reactions	NACRE (Angulo et al. 1999)				
High-T opacities	OPAL (Iglesias & Rogers 1993, 1996)				
Low-T opacities	Ferguson et al. (2005)				
Solar mixture[c]	GS98	AGSS09	AGSS09	GS98	AGSS09
Atmosphere[d]	Eddington gray	Simple photosphere	Simple photosphere	Eddington gray	Kurucz
$\alpha_{\rm MLT}$	1.83	2.175	1.828	2.0	1.7–2.1
Overshoot	Step overshoot[e]	None	None	None	None
Diffusion	Thoul et al. (1994)	None	None	None	None

Notes. One entry is used where all five teams used the same input physics.
[a] The MESA/OPAL tables are based on the 2005 update of the OPAL EoS tables (Rogers & Nayfonov 2002).
[b] The adopted methods for surface correction are Kjeldsen et al. (2008) (KB) and Ball & Gizon (2014) two-term correction (BG-2term).
[c] Solar composition given in Grevesse & Sauval (1998) (GS98) and Asplund et al. (2009) (AGSS09) are used for initial chemical composition.
[d] The atmosphere choices used in MESA are introduced in Paxton et al. (2011), and ASTEC uses the Kurucz model (Kurucz 1991) for the atmosphere.
[e] The overshoot parameters $f_{\rm ov}$ and $f_{0,\ {\rm ov}}$ are set as 0.006 and 0.003. The overshooting is applied at all convective boundaries.
References. Ong: Mier (2017); Kayhan: Kayhan et al. (2019); Izmir: Yıldız et al. (2019); Zhang: Zhang et al. (2022); BESTP: Jiang & Gizon (2021).

Table 4
Modeling Results from Different Sources

Team	Ong	Kayhan	Izmir	Zhang	BESTP
$M_\star$ ($M_\odot$)	1.31 ± 0.06	1.28 ± 0.16	1.15 ± 0.14	1.17 ± 0.01	1.20 ± 0.10
$R_\star$ ($R_\odot$)	8.96 ± 0.14	8.29 ± 0.14	8.62 ± 0.39	8.67 ± 0.02	8.87 ± 0.26
$\log g$ (cgs)	2.650 ± 0.008	2.709 ± 0.002	2.630 ± 0.019	2.630 ± 0.001	2.620 ± 0.010
t (Gyr)	4.1 ± 0.7	4.3 ± 0.5	5.8 ± 2.1	6.3 ± 0.06	5.6 ± 1.4

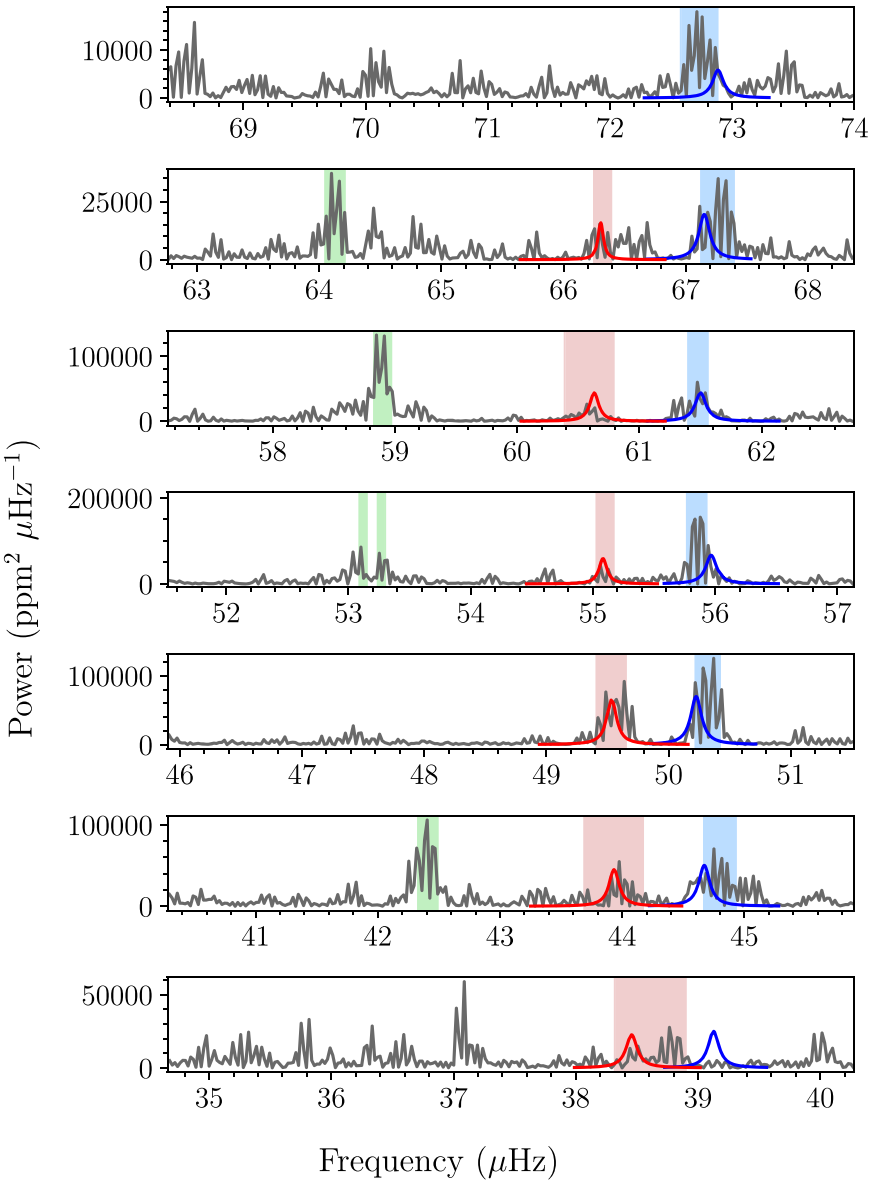

Figure 7. Background-corrected PSD (dark gray) plotted in the échelle diagram format, which divides the spectrum into bins each $\Delta\nu$ wide. The blue and red peaks are the $\ell = 0$ and 2 modes, respectively, of the best-fitting model returned by BESTP (Figure 6). The line width and amplitude of the theoretical modes are derived using the formulae introduced in Lund et al. (2017) and Ball et al. (2018). The corresponding observed frequencies and uncertainties (Table 2) are indicated by the horizontal spans, with additional $\ell = 1$ modes in green.

transit signal was found by Bergmann et al. (2021) or in our data. Thus, we could not measure the planetary orbit or eccentricity through the TESS photometric data.

However, we can combine our newly computed asteroseismic stellar mass ($M_{\star,\mathrm{seis}} = 1.22 \pm 0.11\,M_\odot$) with the orbital period, RV semi-amplitude, and eccentricity values found by Bergmann et al. (2021) to compute updated values for the planet's semimajor axis and minimum mass. Using values from Bergmann et al. (2021), we find $a = 1.165 \pm 0.035$ au and $M_\mathrm{p} \sin i = 3.57 \pm 0.22\,M_\mathrm{Jup}$. These updated parameters place the orbital pericenter of the planet at 0.142 ± 0.005 au, revealing that the planet's orbit is sufficiently far from the star such that tidal decay is currently negligible until the star expands its radius by at least 50%–100% (Villaver & Livio 2009), and subsequently engulfs the planet, in line with the findings of Bergmann et al. (2021).

The time at which the star will engulf the planet will depend on when the star began ascending the RGB. During this phase of stellar evolution, the star's radius will expand to a distance approximately one order of magnitude greater than the planet's orbital pericenter, allowing the star to easily and quickly engulf the planet. For instance, further evolving the best-fitting model (Figure 6) along the evolutionary track, we predict that the expanding star will have a radius one order of magnitude greater than the planet's orbital pericenter and engulf the planet in about 130 Myr.

As an independent estimation of the planetary engulfment time, we also calculated models using the SSE prescription from Hurley et al. (2000). According to this prescription, a $1.22\,M_\odot$ star with a metallicity of $Z = 0.02$ will begin the red giant phase at about 5.58 Gyr and leave it at 6.01 Gyr. During this interval, the planet will be engulfed. Asteroseismology has

allowed us to estimate the current age of the star to be 5.2 ± 1.4 Gyr. This value clearly demonstrates that the star is on the verge of engulfing the planet. However, the uncertainty on the age is about triple the value of the duration of the red giant phase. Nevertheless, asteroseismology has also allowed us to constrain the stellar radius to a value of $8.68 \pm 0.34\,R_{\odot}$. This value corresponds to an age from the SSE model of 5.939 ± 0.004 Gyr, meaning that the planet will be engulfed in less than about 150 Myr. However, this approximate upper bound is likely an overestimate given the fact that the star's metallicity is subsolar.

Other stellar models produce similar results, just renormalized to other absolute ages within the measured asteroseismic uncertainty. For example, a $1.22\,M_{\odot}$ star with a sub-solar metallicity of $Z = 0.01$ will begin the red giant phase at about 4.72 Gyr and leave it at 5.08 Gyr. In this case, the asteroseismically measured radius corresponds to an age from the SSE model of 5.007 ± 0.004 Gyr. This value illustrates that the planet will be engulfed within about 70 Myr. This result is in agreement with that of Bergmann et al. (2021).

6. Conclusions

In this work, we have analyzed the TESS photometric data for HD 76920 to determine the star's fundamental parameters using asteroseismology, and to characterize the exoplanet system consisting of a planet with an extremely large orbital eccentricity. In total, five sectors of the TESS light curves are used for the extraction of asteroseismic parameters for the host star, including 17 individual oscillation frequencies. Modeling by various pipelines that utilize the extracted asteroseismic parameters, classical spectroscopic observables, as well as luminosity from Gaia DR3 parallax, places strong constraints on the stellar parameters. Through the asteroseismic analysis, we obtain a value for the stellar mass of $1.22 \pm 0.11\,M_{\odot}$, a stellar radius of $8.68 \pm 0.34\,R_{\odot}$, and an age of 5.2 ± 1.4 Gyr, which provide the most precise estimations for HD 76920 to date. The stellar models reveal that the star is ascending the RGB and most likely approaching close to the luminosity bump where the properties of mixed modes are significantly impacted by the buoyancy glitch. However, the current power spectrum of HD 76920 from TESS does not allow the extraction of a sufficient number of mixed modes as would be required for the investigation of the buoyancy glitch.

The updated stellar parameters of the host star from our asteroseismic analysis have enabled improved estimations for the semimajor axis and mass of the planet as $a = 1.165 \pm 0.035$ au and $M_{\rm p} \sin i = 3.57 \pm 0.22\,M_{\rm Jup}$. With an orbital pericenter of 0.142 ± 0.005 au, we confirm that the planet is currently far away enough from the star to experience negligible tidal decay before being engulfed in the stellar envelope. However, we predict that this event will occur within about 100 Myr, depending on the stellar model used.

HD 76920 will be observed in five more sectors by TESS in Cycle 5. The prolonged data will possibly enable the detection of mixed modes, and thus, the investigation of stellar interior through these modes. Moreover, our asteroseismic analysis emphasizes the potential of TESS for characterizing exoplanet systems through the synergy between exoplanet research and asteroseismology.

The project leading to this publication has received funding from the B-type Strategic Priority Program of the Chinese Academy of Sciences (grant No. XDB41000000). A.D.F. acknowledges the support from the National Science Foundation Graduate Research Fellowship Program under grant No. (DGE-1746045). M.S.L. would like to acknowledge the support from VILLUM FONDEN (research grant 42101) and The Independent Research Fund Denmark's Inge Lehmann program (grant agreement No.: 1131-00014B). C.K. is supported by Erciyes University Scientific Research Projects Coordination Unit under grant No. DOSAP MAP-2020-9749. T.W. acknowledges the support from the National Key Research and Development Program of China (grant No. 2021YFA1600402), the National Natural Science Foundation of China (grant Nos. 11873084, 12133011, and 12273104), the Youth Innovation Promotion Association of Chinese Academy of Sciences, and the Ten Thousand Talents Program of Yunnan for Top-notch Young Talents. X.-Y.Z. acknowledges the support from the National Natural Science Foundation of China (grant No. 12173105). S. M. acknowledges the support from the Spanish Ministry of Science and Innovation (MICINN) with the Ramón y Cajal fellowship No. RYC-2015-17697, grant Nos. PID2019-107187GB-I00 and PID2019-107061GB-C66, and through AEI under the Severo Ochoa Centres of Excellence Program 2020–2023 (CEX2019-000920-S). R.A.G. and S.N.B. acknowledge the support from PLATO and GOLF CNES grants. S.N.B acknowledges support from PLATO ASI-INAF agreement No. 2015-019-R.1-2018. This work was also supported by Fundação para a Ciência e a Tecnologia (FCT) through research grants UIDB/04434/2020 and UIDP/04434/2020. T.L.C. and M.S.C. are supported by FCT in the form of a work contract (CEECIND/00476/2018, CEECIND/02619/2017). D.H. acknowledges support from the Alfred P. Sloan Foundation and the National Aeronautics and Space Administration (80NSSC21K0652, 80NSSC20K0593).

Facilities: TESS, Gaia.

Software: `eleanor` (Feinstein et al. 2019), `lightkurve` (Lightkurve Collaboration et al. 2018), `TessCut` (Brasseur et al. 2019), `LAURA` (De Moura et al. 2020), `FAMED` (Corsaro et al. 2020), `echelle`, `SolarlikePeakbagging` (Li et al. 2020), `apollinaire` (Breton et al. 2022), `fnpeaks`, `SYD` (Huber et al. 2009), `A2Z` (Mathur et al. 2010), `Period04` (Lenz & Breger 2005), `Yabox` (Mier 2017), `SEDEX` (Yu et al. 2021, 2023).

ORCID iDs

Chen Jiang (姜晨) https://orcid.org/0000-0002-7614-1665
Tao Wu (吴涛) https://orcid.org/0000-0001-6832-4325
Adina D. Feinstein https://orcid.org/0000-0002-9464-8101
Keivan G. Stassun https://orcid.org/0000-0002-3481-9052
Timothy R. Bedding https://orcid.org/0000-0001-5222-4661
Dimitri Veras https://orcid.org/0000-0001-8014-6162
Enrico Corsaro https://orcid.org/0000-0001-8835-2075
Derek L. Buzasi https://orcid.org/0000-0002-1988-143X
Dennis Stello https://orcid.org/0000-0002-4879-3519
Yaguang Li (李亚光) https://orcid.org/0000-0003-3020-4437
Savita Mathur https://orcid.org/0000-0002-0129-0316
Rafael A. García https://orcid.org/0000-0002-8854-3776
Sylvain N. Breton https://orcid.org/0000-0003-0377-0740
Mia S. Lundkvist https://orcid.org/0000-0002-8661-2571
Przemysław J. Mikołajczyk https://orcid.org/0000-0001-8916-8050
Charlotte Gehan https://orcid.org/0000-0002-0833-7084

Tiago L. Campante https://orcid.org/0000-0002-4588-5389
Diego Bossini https://orcid.org/0000-0002-9480-8400
Stephen R. Kane https://orcid.org/0000-0002-7084-0529
Jia Mian Joel Ong (王加冕) https://orcid.org/0000-0001-7664-648X
Mutlu Yıldız https://orcid.org/0000-0002-7772-7641
Cenk Kayhan https://orcid.org/0000-0001-9198-2289
Zeynep Çelik Orhan https://orcid.org/0000-0002-9424-2339
Sibel Örtel https://orcid.org/0000-0001-5759-7790
Xinyi Zhang (张昕旖) https://orcid.org/0000-0003-1860-1851
Margarida S. Cunha https://orcid.org/0000-0001-8237-7343
Bruno Lustosa de Moura https://orcid.org/0000-0001-6295-3526
Jie Yu (余杰) https://orcid.org/0000-0002-0007-6211
Daniel Huber https://orcid.org/0000-0001-8832-4488
Jian-wen Ou (欧建文) https://orcid.org/0000-0002-6176-7745
Robert A. Wittenmyer https://orcid.org/0000-0001-9957-9304
Laurent Gizon https://orcid.org/0000-0001-7696-8665
William J. Chaplin https://orcid.org/0000-0002-5714-8618

References

Adamów, M., Niedzielski, A., Kowalik, K., et al. 2018, A&A, 613, A47
Adamów, M., Niedzielski, A., Villaver, E., Nowak, G., & Wolszczan, A. 2012, ApJL, 754, L15
Anders, F., Chiappini, C., Minchev, I., et al. 2017, A&A, 600, A70
Angulo, C., Arnould, M., Rayet, M., et al. 1999, NuPhA, 656, 3
Appourchaux, T., Chaplin, W. J., García, R. A., et al. 2012, A&A, 543, A54
Asplund, M., Grevesse, N., Sauval, A. J., & Scott, P. 2009, ARA&A, 47, 481
Baglin, A., Auvergne, M., Boisnard, L., et al. 2006, in 36th COSPAR Scientific Assembly, Meeting abstract from the CDROM (Washington, DC: NASA), 3749
Ball, W. H., Chaplin, W. J., Schofield, M., et al. 2018, ApJS, 239, 34
Ball, W. H., & Gizon, L. 2014, A&A, 568, A123
Ballard, S., Chaplin, W. J., Charbonneau, D., et al. 2014, ApJ, 790, 12
Beck, P. G., Montalban, J., Kallinger, T., et al. 2012, Natur, 481, 55
Bedding, T. R., & Kjeldsen, H. 2010, CoAst, 161, 3
Bedding, T. R., Kjeldsen, H., Arentoft, T., et al. 2007, ApJ, 663, 1315
Bedding, T. R., Mosser, B., Huber, D., et al. 2011, Natur, 471, 608
Benomar, O., Masuda, K., Shibahashi, H., & Suto, Y. 2014, PASJ, 66, 94
Bergmann, C., Jones, M. I., Zhao, J., et al. 2021, PASA, 38, E019
Borucki, W. J., Koch, D., Basri, G., et al. 2010, Sci, 327, 977
Brasseur, C. E., Phillip, C., Fleming, S. W., Mullally, S. E., & White, R. L. 2019, Astrocut: Tools for Creating Cutouts of TESS Images, Astrophysics Source Code Library, ascl:1905.007
Breton, S. N., García, R. A., Ballot, J., Delsanti, V., & Salabert, D. 2022, A&A, 663, A118
Brown, T. M., Gilliland, R. L., Noyes, R. W., & Ramsey, L. W. 1991, ApJ, 368, 599
Campante, T. L., Barclay, T., Swift, J. J., et al. 2015, ApJ, 799, 170
Campante, T. L., Barros, S. C. C., Demangeon, O., et al. 2018, in PHysics of Oscillating STars. Proc. from the PHOST (PHysics of Oscillating STars) Symp. (Zenodo), 50
Campante, T. L., Corsaro, E., Lund, M. N., et al. 2019, ApJ, 885, 31
Campante, T. L., Lund, M. N., Kuszlewicz, J. S., et al. 2016a, ApJ, 819, 85
Campante, T. L., Schofield, M., Kuszlewicz, J. S., et al. 2016b, ApJ, 830, 138
Campante, T. L., Veras, D., North, T. S. H., et al. 2017, MNRAS, 469, 1360
Casagrande, L., Silva Aguirre, V., Stello, D., et al. 2014, ApJ, 787, 110
Casagrande, L., Silva Aguirre, V., Schlesinger, K. J., et al. 2016, MNRAS, 455, 987
Chaplin, W. J., Basu, S., Huber, D., et al. 2014, ApJS, 210, 1
Christensen-Dalsgaard, J. 2008a, Ap&SS, 316, 13
Christensen-Dalsgaard, J. 2008b, Ap&SS, 316, 113
Claret, A., & Torres, G. 2017, ApJ, 849, 18
Claret, A., & Torres, G. 2018, ApJ, 859, 100
Claret, A., & Torres, G. 2019, ApJ, 876, 134
Corsaro, E., & De Ridder, J. 2014, A&A, 571, A71
Corsaro, E., De Ridder, J., & García, R. A. 2015, A&A, 579, A83
Corsaro, E., McKeever, J. M., & Kuszlewicz, J. S. 2020, A&A, 640, A130
Corsaro, E., Mathur, S., García, R. A., et al. 2017, A&A, 605, A3
Cunha, M. S., Avelino, P. P., Christensen-Dalsgaard, J., et al. 2019, MNRAS, 490, 909
Cunha, M. S., Stello, D., Avelino, P. P., Christensen-Dalsgaard, J., & Townsend, R. H. D. 2015, ApJ, 805, 127
Davies, G. R., & Miglio, A. 2016, AN, 337, 774
Dawson, R. I., & Johnson, J. A. 2018, ARA&A, 56, 175
De Moura, B. L., Beck, P. G., Di Mauro, M. P., et al. 2020, ApJ, 894, 67
Feinstein, A. D., Montet, B. T., Foreman-Mackey, D., et al. 2019, PASP, 131, 094502
Ferguson, J. W., Alexander, D. R., Allard, F., et al. 2005, ApJ, 623, 585
Frink, S., Mitchell, D. S., Quirrenbach, A., et al. 2002, ApJ, 576, 478
Gaia Collaboration, Brown, A. G. A., Vallenari, A., et al. 2021, A&A, 649, A1
Gilliland, R. L., McCullough, P. R., Nelan, E. P., et al. 2011, ApJ, 726, 2
Grevesse, N., & Sauval, A. J. 1998, SSRv, 85, 161
Guo, F., & Li, Y. 2019, ApJ, 879, 86
Gustafsson, B., Edvardsson, B., Eriksson, K., et al. 2008, A&A, 486, 951
Handberg, R., Brogaard, K., Miglio, A., et al. 2017, MNRAS, 472, 979
Handberg, R., & Campante, T. L. 2011, A&A, 527, A56
Harvey, J. 1985, in Future Missions in Solar, Heliospheric Space Plasma Physics, Proc. ESA Special Publ., Vol. 235,, ed. E. Rolfe & B. Battrick (Noordwijk: ESA Scientific & Technical), 199
Hatt, E., Nielsen, M. B., Chaplin, W. J., et al. 2023, A&A, 669, A67
Hekker, S., Broomhall, A. M., Chaplin, W. J., et al. 2010, MNRAS, 402, 2049
Hill, M. L., Kane, S. R., Campante, T. L., et al. 2021, AJ, 162, 211
Houdek, G., Trampedach, R., Aarslev, M. J., & Christensen-Dalsgaard, J. 2017, MNRAS Lett., 464, L124
Houk, N., & Cowley, A. P. 1975, University of Michigan Catalog of Two-dimensional Spectral Types for the HD Stars. Vol. I. Declinations −90°.0 to −53°.0 (Ann Arbor, MI: Univ. of Michigan)
Huber, D. 2018, Asteroseismology and Exoplanets: Listening to the Stars and Searching for New Worlds, Astrophysics and Space Science Proceedings, Vol. 49 (Cham: Springer), 119
Huber, D., Carter, J. A., Barbieri, M., et al. 2013, Sci, 342, 331
Huber, D., Chaplin, W. J., Chontos, A., et al. 2019, AJ, 157, 245
Huber, D., Stello, D., Bedding, T. R., et al. 2009, CoAst, 160, 74
Huber, D., White, T. R., Metcalfe, T. S., et al. 2022, AJ, 163, 79
Hurley, J. R., Pols, O. R., & Tout, C. A. 2000, MNRAS, 315, 543
Iglesias, C. A., & Rogers, F. J. 1993, ApJ, 412, 752
Iglesias, C. A., & Rogers, F. J. 1996, ApJ, 464, 943
Jenkins, J. M., Twicken, J. D., McCauliff, S., et al. 2016, Proc. SPIE, 9913, 99133E
Jiang, C. 2015, PhD thesis, Aarhus Univ.
Jiang, C., Bedding, T. R., Stassun, K. G., et al. 2020b, ApJ, 896, 65
Jiang, C., Cunha, M., Christensen-Dalsgaard, J., & Zhang, Q. 2020a, MNRAS, 495, 621
Jiang, C., Cunha, M., Christensen-Dalsgaard, J., Zhang, Q. S., & Gizon, L. 2022, MNRAS, 515, 3853
Jiang, C., & Gizon, L. 2021, RAA, 21, 226
Jiang, C., Jiang, B. W., Christensen-Dalsgaard, J., et al. 2011, ApJ, 742, 120
Kallinger, T., Beck, P. G., Stello, D., & Garcia, R. A. 2018, A&A, 616, A104
Kallinger, T., De Ridder, J., Hekker, S., et al. 2014, A&A, 570, A41
Kallinger, T., Hekker, S., Mosser, B., et al. 2012, A&A, 541, A51
Kallinger, T., Weiss, W. W., Barban, C., et al. 2010, A&A, 509, A77
Kamiaka, S., Benomar, O., Suto, Y., et al. 2019, AJ, 157, 137
Kane, S. R., Bean, J. L., Campante, T. L., et al. 2021, PASP, 133, 014402
Kane, S. R., Ciardi, D. R., Gelino, D. M., & von Braun, K. 2012, MNRAS, 425, 757
Kane, S. R., Reffert, S., Henry, G. W., et al. 2010, ApJ, 720, 1644
Karoff, C. 2008, PhD thesis, Aarhus Univ.
Kayhan, C., Yıldız, M., & Çelik Orhan, Z. 2019, MNRAS, 490, 1509
Kjeldsen, H., & Bedding, T. R. 1995, A&A, 293, 87
Kjeldsen, H., Bedding, T. R., Butler, R. P., et al. 2005, ApJ, 635, 1281
Kjeldsen, H., Bedding, T. R., & Christensen-Dalsgaard, J. 2008, ApJL, 683, L175
Kurucz, R. L. 1991, in Stellar Atmospheres: Beyond Classical Models, ed. L. Crivellari et al., Vol. 341 (Dordrecht: Reidel), 441
Lenz, P., & Breger, M. 2005, CoAst, 146, 53
Li, Y., Bedding, T. R., Li, T., et al. 2020, MNRAS, 495, 2363
Lightkurve Collaboration, Cardoso, J. V. D. M., Hedges, C., et al. 2018, Lightkurve: Kepler and TESS time series analysis in Python, Astrophysics Source Code Library, ascl:1812.013
Lindsay, C. J., Ong, J. M. J., & Basu, S. 2022, ApJ, 931, 116
Lund, M. N., Lundkvist, M., Silva Aguirre, V., et al. 2014, A&A, 570, A54
Lund, M. N., Silva Aguirre, V., Davies, G. R., et al. 2017, ApJ, 835, 172
Lundkvist, M. S. 2015, PhD thesis, Aarhus Univ.
Lundkvist, M. S., Kjeldsen, H., Albrecht, S., et al. 2016, NatCo, 7, 11201

Mathur, S., García, R. A., Régulo, C., et al. 2010, A&A, 511, A46
Mathur, S., Metcalfe, T. S., Woitaszek, M., et al. 2012, ApJ, 749, 152
Metcalfe, T. S., Monteiro, M. J. P. F. G., Thompson, M. J., et al. 2010, ApJ, 723, 1583
Mier, P. R. 2017, Pablormier/Yabox: V1.0.3, v1.0.3, Zenodo, doi:10.5281/zenodo.848679
Mosser, B., & Appourchaux, T. 2009, A&A, 508, 877
Mosser, B., Goupil, M. J., Belkacem, K., et al. 2012, A&A, 540, A143
Nielsen, M. B., Ball, W. H., Standing, M. R., et al. 2020, A&A, 641, A25
Ong, J. M. J., & Basu, S. 2020, ApJ, 898, 127
Ong, J. M. J., Basu, S., & McKeever, J. M. 2021, ApJ, 906, 54
Paxton, B., Bildsten, L., Dotter, A., et al. 2011, ApJS, 192, 3
Paxton, B., Cantiello, M., Arras, P., et al. 2013, ApJS, 208, 4
Paxton, B., Marchant, P., Schwab, J., et al. 2015, ApJS, 220, 15
Pinćon, C., Goupil, M. J., & Belkacem, K. 2020, A&A, 634, A68
Pinsonneault, M. H., Elsworth, Y., Epstein, C., et al. 2014, ApJS, 215, 19
Pinsonneault, M. H., Elsworth, Y. P., Tayar, J., et al. 2018, ApJS, 239, 32
Rendle, B. M., Buldgen, G., Miglio, A., et al. 2019, MNRAS, 484, 771
Ricker, G. R., Winn, J. N., Vanderspek, R., et al. 2015, JATIS, 1, 014003
Rodrigues, T. S., Girardi, L., Miglio, A., et al. 2014, MNRAS, 445, 2758
Rogers, F. J., & Nayfonov, A. 2002, ApJ, 576, 1064
Roxburgh, I. W. 2017, A&A, 604, A42
Schlegel, D. J., Finkbeiner, D. P., & Davis, M. 1998, ApJ, 500, 525
Schofield, M., Chaplin, W. J., Huber, D., et al. 2019, ApJS, 241, 12
Serenelli, A., Johnson, J., Huber, D., et al. 2017, ApJS, 233, 23
Sharma, S., Stello, D., Bland-Hawthorn, J., Huber, D., & Bedding, T. R. 2016, ApJ, 822, 15
Silva Aguirre, V., Casagrande, L., Basu, S., et al. 2012, ApJ, 757, 99
Silva Aguirre, V., Lund, M. N., Antia, H. M., et al. 2017, ApJ, 835, 173
Silva Aguirre, V., Stello, D., Stokholm, A., et al. 2020, ApJL, 889, L34
Sliski, D. H., & Kipping, D. M. 2014, ApJ, 788, 148
Stassun, K. G., Collins, K. A., & Gaudi, B. S. 2017, AJ, 153, 136
Stassun, K. G., Corsaro, E., Pepper, J. A., & Gaudi, B. S. 2018a, AJ, 155, 22
Stassun, K. G., Oelkers, R. J., Pepper, J., et al. 2018b, AJ, 156, 102
Stassun, K. G., & Torres, G. 2016, AJ, 152, 180
Stassun, K. G., & Torres, G. 2021, ApJL, 907, L33
Stello, D., Bruntt, H., Preston, H., & Buzasi, D. 2008, ApJL, 674, L53
Stello, D., Meibom, S., Gilliland, R. L., et al. 2011, ApJ, 739, 13
Thoul, A. A., Bahcall, J. N., & Loeb, A. 1994, ApJ, 421, 828
Torres, G., Andersen, J., & Giménez, A. 2010, A&ARv, 18, 67
Townsend, R. H. D., & Teitler, S. A. 2013, MNRAS, 435, 3406
Van Eylen, V., & Albrecht, S. 2015, ApJ, 808, 126
Van Eylen, V., Albrecht, S., Huang, X., et al. 2019, AJ, 157, 61
van Leeuwen, F. 2007, A&A, 474, 653
Viani, L. S., Basu, S., Corsaro, E., Ball, W. H., & Chaplin, W. J. 2019, ApJ, 879, 33
Villaver, E., & Livio, M. 2009, ApJL, 705, L81
Vrard, M., Mosser, B., Barban, C., et al. 2015, A&A, 579, A84
Wittenmyer, R. A., Jones, M. I., Horner, J., et al. 2017, AJ, 154, 274
Wu, T., & Li, Y. 2016, ApJL, 818, L13
Wu, T., & Li, Y. 2017, ApJ, 846, 41
Wu, T., & Li, Y. 2019, ApJ, 881, 86
Yıldız, M., Çelik Orhan, Z., & Kayhan, C. 2019, MNRAS, 489, 1753
Yu, J., Hekker, S., Bedding, T. R., et al. 2021, MNRAS, 501, 5135
Yu, J., Huber, D., Bedding, T. R., et al. 2018, ApJS, 236, 42
Yu, J., Khanna, S., Themessl, N., et al. 2023, ApJS, 264, 41
Zhang, X., Cai, T., Li, Y., & Wu, T. 2022, ApJ, 931, 64
Zhang, X., Li, Y., Wu, T., & Su, J. 2020, MNRAS, 494, 511
Zhang, X., Wu, T., & Li, Y. 2018, ApJ, 855, 16